

# Quantifying the Effect of Basic Minerals on Acid- and Ligand-Promoted Dissolution Kinetics of Iron in Simulated Dark Atmospheric Aging of Dust and Coal Fly Ash Particles

Published as part of *The Journal of Physical Chemistry A* special issue "Vicki H. Grassian Festschrift".

Hind A. Al-Abadleh,\* Madison Smith, Arden Ogilvie, and Nausheen W. Sadiq\*



Cite This: *J. Phys. Chem. A* 2024, 128, 8198–8208



Read Online

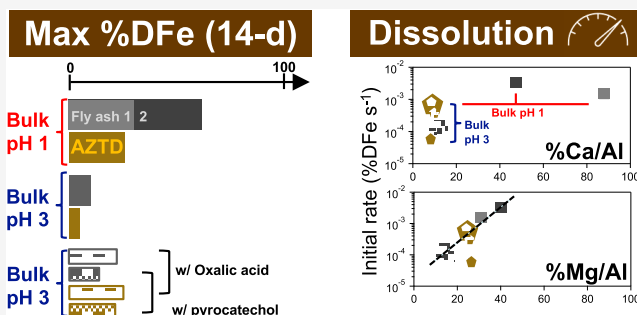
ACCESS |

Metrics & More

Article Recommendations

Supporting Information

**ABSTRACT:** The content and multiphase chemistry of iron (Fe) in multicomponent atmospheric aerosols are important to global climate and oceanic models. To date, reported dissolution rates of Fe span orders of magnitude with no quantifiable dependency on the content of basic minerals that coexist with Fe. Here, we report dissolution rates of Fe in simulated dark atmospheric aging of fully characterized multielement particles under acidic conditions (bulk pH 1 or 3) with and without oxalic acid and pyrocatechol. Our main findings are (a) the total amount of Ca and Mg was higher in coal fly ash than in Arizona test dust, (b) Fe dissolution initial rates increased exponentially with %Ca/Al and %Mg/Al below 50%, (c) a reduction in the Fe dissolution initial rate was observed with %Ca/Al higher than 50%, (d) reactive Ca and Mg minerals increased the calculated initial pH at the liquid/solid interface to values higher by only 1.5–2 units than the measured bulk pH, yet interfacial water remained acidic for Fe dissolution to take place, and (e) reactive Ca and Mg minerals enhanced the deprotonation of organics at the interface, aiding in ligand-promoted dissolution of Fe. The impact of these results is discussed within the context of constraining Fe dissolution kinetic models.



## INTRODUCTION

Atmospheric aerosol aging refers to the processes that change aerosol physicochemical properties during their atmospheric long-range transport, which can last up to 2 weeks.<sup>1,2</sup> These processes take place within the aerosol condensed phase or at the surface of the particles/droplets.<sup>3–5</sup> The extent and rates of these reactions are influenced by the aerosol water content that affects aerosol acidity and ionic strength.<sup>6,7</sup> Aging of aerosol particles changes their chemical composition, mixing state, morphology, and optical properties, which impact radiative forcing and ice/cloud nucleation efficiency and hence directly and indirectly aerosol–radiation and aerosol–cloud interactions. However, the representation and multiphase chemistry of iron (Fe)-containing aerosol from mineral dust, combustion fly ash, and wildfire aerosol from natural and anthropogenic sources remain limited in atmospheric models, particularly under aerosol liquid water conditions.<sup>4,8–10</sup>

Fe-containing minerals in atmospheric aerosols are also of importance to understanding iron's role as a micronutrient.<sup>11–15</sup> At a molecular level, aerosols containing Fe deposited on the sea surface microlayer (SML) experience a heterogeneous chemical environment characterized by mixtures of organic matter with ligands having a wide range of complexation affinity to Fe.<sup>16,17</sup> Also, at the SML, the pH

changes from the acidic values in aerosol liquid water to more basic. When combined with changes in salinity, the deposited Fe would change phases and speciation, with impacts on the rates of dissolution, aggregation, and complexation to organic and inorganic ligands. The rates of these processes are also affected by sunlight at the sea and ocean surface, which further complicates our understanding of Fe fate and bioavailability. Yet, life thrives at the SML, and marine primary production is responsible for the capture of up to 35% of the carbon emitted to the atmosphere by human activities.<sup>18</sup> This is because phytoplankton species employ *in situ* biological Fe uptake by either excreting siderophores to mobilize Fe from particulate matter or developing cell-surface processes that enhance Fe dissolution from oxides and dust.<sup>9</sup> Despite our current understanding of the processes that lead to Fe dissolution at the SML, there are still knowledge gaps that need to be addressed to enhance the predictive power of ocean

Received: July 31, 2024

Revised: September 2, 2024

Accepted: September 9, 2024

Published: September 17, 2024

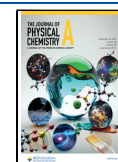


**Table 1. Calcium (Ca) and Magnesium (Mg) Minerals Identified in the Dust and Coal Fly Ash Samples Used Here by X-ray Diffraction (XRD)**

solid material (Fe ( $\mu\text{g g}^{-1}$ ) $\times 10^3$ )	Ca minerals <sup>a</sup> ( $(\mu\text{g g}^{-1}) \times 10^3$ ) <sup>b</sup>	Mg minerals <sup>c</sup> ( $(\mu\text{g g}^{-1}) \times 10^3$ ) <sup>b</sup>
AZTD (36)	albite ( $\text{Na}_{0.98}\text{Ca}_{0.02}\text{Al}_{1.02}\text{Si}_{2.98}\text{O}_8$ , 34%), calcite ( $\text{CaCO}_3$ , 8%) (3.8)	magnesium oxide ( $\text{MgO}$ , 10%), magnesite ( $\text{MgCO}_3$ , 7%), enstatite ( $\text{Mg}_{1.79}\text{Fe}_{0.21}(\text{Si}_2\text{O}_6)$ ) (42%), augite ( $\text{Ca}(\text{Mg},\text{Fe})\text{Si}_2\text{O}_6$ ) (42%) (12)
INFA (26)	<sup>d</sup> (1.9)	magnesium oxide ( $\text{MgO}$ , 26%), magnesite ( $\text{MgCO}_3$ , 74%) (2.2)
USFA (36)	anhydrite ( $\text{CaSO}_4$ , 39%), calcite ( $\text{CaCO}_3$ , 35%) (28)	magnesium oxide ( $\text{MgO}$ , 10%), magnesite ( $\text{MgCO}_3$ , 55%), augite ( $\text{Ca}(\text{Mg},\text{Fe})\text{Si}_2\text{O}_6$ , 35%) (24)
EUFA (11)	anhydrite ( $\text{CaSO}_4$ , 27%), calcite and vaterite ( $\text{CaCO}_3$ , 31%), calcium aluminum oxide ( $\text{Ca}_3\text{Al}_2\text{O}_6$ , 3%) (31)	magnesium oxide ( $\text{MgO}$ , 59%), magnesite ( $\text{MgCO}_3$ , 41%) (11)

<sup>a</sup>Table 1 in ref 36. The percentages are reported here for the first time relative to the majority of the crystalline mineral phases identified containing Si, Fe, Cu, Pb, and Mn. <sup>b</sup>Table S5 in ref 36 from strong acid extraction. These values were normalized to the surface area in Table S1. Similar values for Fe and Al are also listed there. <sup>c</sup>This work. Because of the complexity of these dust and fly ash samples, the percentages are rough semiquantitative among the identified major crystalline Mg-containing minerals only to get a total % equal to 100%. <sup>d</sup>No crystalline Ca-containing phases were detected. Reproduced with permission from ref 36, which is a publication licensed for personal use by The American Chemical Society. Copyright 2023 American Chemical Society.

biogeochemistry models.<sup>12,13</sup> One of the gaps is related to how fast the dissolved fraction of Fe in “aged” Fe-containing multicomponent aerosols from natural and anthropogenic sources changes in quantity and speciation upon deposition on the SML.<sup>9</sup>

Fe is a redox-(photo)active element in multicomponent atmospheric aerosols. Its surface and bulk aqueous speciation, chemistry, and dissolution kinetics from field and lab dust and Fe-(oxyhydr)oxides were studied extensively under acidic conditions, mimicking the acidity of aerosol liquid water.<sup>3,6</sup> These studies highlighted the range of Fe reactions with water-soluble aerosol components that lead, in most cases, to in situ production of reactive oxygen species (ROS) and secondary organic and inorganic compounds. In addition, some of these reactions lead to the dissolution of Fe from the solid matrix of Fe-containing minerals in atmospheric aerosol particles. Proton-, ligand-, and reductive-promoted dissolution mechanisms are the three main pathways that lead to Fe mobilization.<sup>19–21</sup> A number of variables play a role in these mechanisms, namely, pH, particle size, degree of particle aggregation, crystallinity of Fe-containing minerals, presence of solar radiation, and adsorption mode of Fe-organic complexes.<sup>22–27</sup> A general conclusion from studies over the past four decades is that the highest rates of dissolution occur under acidic conditions<sup>28,29</sup> ( $\text{pH} < 4$ ), in the presence of solar radiation and oxalate, with nanometer size and amorphous Fe-containing particles, especially those originating from combustion sources, which contain higher ratios of Fe(III) than the more soluble Fe(II) relative to the bulk Fe.<sup>30–32</sup>

Despite these advances in our understanding of Fe mobilization in aerosols, few laboratories investigated the effects of basic and amphoteric minerals—that coexist with Fe minerals in dust—on the dissolution kinetics of Fe. For example, Hettiarachchi et al.<sup>33</sup> showed that a Kalahari Desert dust sample with high Ti content resulted in a higher fraction of dissolved Fe(II) under acidic and dark conditions over 50 h. These results agreed with those using hematite ( $\alpha\text{-Fe}_2\text{O}_3$ ) mixed with  $\text{TiO}_2$ , which were followed by a detailed mechanistic study on the dissolution mechanism with varying experimental conditions.<sup>34</sup> However, mixing hematite with  $\text{Al}_2\text{O}_3$  and  $\text{CaO}$  suppressed Fe dissolution from hematite, which was attributed to their inherent basic properties that increased the bulk pH.<sup>33</sup> The reported increase was by 0.1–0.5 pH units above the starting value of 2 compared to a decrease by 0.2 pH units in the case of  $\text{TiO}_2$ .<sup>33</sup> Similar studies were

reported using ilmenite ( $\text{FeTiO}_3$ ).<sup>35</sup> We recently reported the change in the measured bulk pH of dust and coal fly ash as a function of time over 14 days of simulated atmospheric aging experiments at pH 1, 3, 7, and 9.<sup>36</sup> While the pH values changed by  $\pm 0.1$ –0.3 for starting pH 1, the pH change was much higher, ranging from 3 to 10.6 for starting pH 7, particularly for the slurries of two fly ash samples containing statistically significant higher amounts of dissolved calcium (Ca) and magnesium (Mg) by factors ranging from 2 to 6 under acidic and neutral experimental conditions.<sup>36</sup> These studies highlighted the need to quantify the contribution of basic minerals in natural and anthropogenic dust to the Fe dissolution kinetics.

Close examination of the reported dissolution kinetic rates of Fe from field dust and pure Fe-(oxyhydr)oxides shows orders of magnitude differences in their values.<sup>19,31,33–35,37,38</sup> While most of these studies acknowledged the relatively fast and slow Fe dissolution kinetic regimes, the lab experiments were designed at either short time frames (minutes to hours) or longer time periods from hours to days. The lack in uniformity in the experimental conditions among different laboratories can also affect measured dissolved values of Fe as recently highlighted in a related intercomparison study on aerosol trace element solubility from four different leaching protocols.<sup>39</sup> Hence, it is challenging to derive a single dissolution kinetic model that captures rate changes with atmospherically relevant time periods and its dependence on (a) the key physical and chemical properties of Fe-containing materials and (b) the experimental conditions simulating aerosol liquid water.

The main objective of our laboratory study here is to quantify the effect of basic minerals containing Ca and Mg on the dissolution kinetics of Fe in simulated acidic and dark atmospheric aging of fully characterized multielement reference solid materials representative of atmospheric aerosol particles from natural and combustion sources. More specifically, we quantified the dependency of the initial dissolution rates (from modeling data points on day 1) and fast and slow rate constants (from modeling the full data set) on bulk pH and the total content of Ca and Mg normalized to aluminum (Al). As detailed below, the results reported here using reference materials would be used as benchmarks to aid in designing and interpreting data from future kinetic experiments and analysis of field filters aimed at constraining atmospheric aerosol and ocean biogeochemistry models.

## EXPERIMENTAL AND KINETIC MODELING METHODS

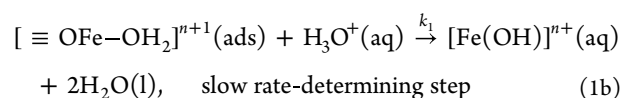
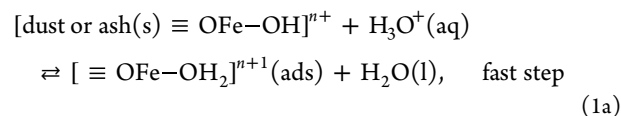
**Chemicals.** All chemicals were used as received without further purification: Arizona Test Dust (AZTD, Powder Technology, Inc., 0–3  $\mu\text{m}$  nominal particle size, ~5% (w/w) Fe)<sup>40</sup> and coal fly ash samples received from Prof. Juan Navea: India Fly Ash (INFA), United States Fly Ash (USFA), and European Fly Ash (EUFA) (see refs 36,41,42 for comprehensive materials characterization of each fly ash), oxalic acid dihydrate (Ox, 99%, CAS: 6153-56-6, Sigma-Aldrich), pyrocatechol (CAT,  $\geq 99\%$ , CAS: 120-80-9, Sigma-Aldrich), and diluted hydrochloric acid (HCl, 6 M, Ricca Chemical Company). Dust or fly ash slurries were prepared by suspending the solids in Milli-Q water (18.2 M $\Omega$ -cm). Table 1 lists Ca and Mg minerals with their semiquantitative relative abundance from X-ray diffraction (XRD). The total amounts of these elements from strong acid extraction are also listed. Additional amounts for Fe and Al are listed in Table S1.

**Simulated Atmospheric Aging Experiments.** These time-dependent experiments were conducted using AZTD and fly ash (INFA, USFA, and EUFA) under dark acidic conditions at room temperature (298 K). AZTD is used here as a standard dust benchmark, given its commercial availability, so that the results from field-collected particles by other research groups could be compared to it. The initial bulk pH was either  $1 \pm 0.1$  or  $3 \pm 0.1$ , with or without organics (oxalic acid or pyrocatechol), as indicated in the Results and Discussion section. Both of these pH values are below the minimum pH range of 3.5–4.5 needed for precipitating Fe ions as hydroxides.<sup>43</sup> Each data point in the dissolved Fe kinetic curve was obtained from analyzing 1–3 vials to obtain a minimum of 13 time points from 00:00 until 14 days. Each vial contained  $5 \pm 0.1$  mg of solid material and 5 mL total solution volume for a slurry concentration of 1 g L<sup>-1</sup>. This solid/liquid ratio is typical for experiments simulating dust aging in aerosol liquid water and relevant for dust ice nucleation lab experiments.<sup>40</sup> Vials were placed horizontally and shaken at 120 rpm using a Thermo Scientific MAXQ 6000 instrument throughout the duration of the experiment. The final bulk pH was measured at each time point. At a given time point, the slurries were filtered using syringe filters (0.2  $\mu\text{m}$  nylon filters, 25 mm diameter, Fisherbrand Basix), and the filtrates were analyzed using inductively coupled plasma mass spectrometry (ICP-MS) for the concentration of dissolved Fe (DFe). We adopt the term “dissolved” following the recommendation by Meskhidze et al.<sup>12</sup> for the species of trace elements that pass through the 0.2  $\mu\text{m}$  pores. For experiments using organics Ox and CAT, the final concentration in each vial was 1 mM. The atmospheric relevance of the slurry and organics concentrations used here was provided earlier in ref 36 in relation to deliquesced aerosol. Additional details on the experimental methods are provided in the Supporting Information (SI).

**Elemental Analysis Using ICP-MS.** To obtain the dissolution kinetic curves of Fe from the solids, samples were analyzed using the EPA method 6020B (mod) following sample preparation with strong acid (HNO<sub>3</sub>/HCl) extractions using the EPA method 200.2 (mod). Total metal analysis was conducted using an Agilent 7850 ICP-MS instrument equipped with High Matrix Introduction (HMI) mode, a helium collision cell, and a Burgener Mira Mist Nebulizer for metal analysis. External calibration was utilized, with the preparation of a multielemental calibration curve spanning

0.1–100 ppm (Inorganic Ventures). Additional details are provided in the SI.

**Dissolution Kinetics Modeling.** The fast and slow dissolution kinetics model containing two rate constants was derived for the following reactions at pH 1 and 3 for acid-promoted and ligand-promoted reactions. At pH 1 (with no organics),



where  $n+$  is net positive charge on the pH-dependent speciation of Fe. Equation 2 is the simplified rate equation derived from reactions 1a and 1b for acid-promoted dissolution as detailed in the SI:

$$\frac{d[\text{DFe}]}{dt} = k_1 \cdot [\text{H}_3\text{O}^+(\text{aq})]_0 e^{-k_1 t} \quad (2)$$

Equations 1 and 2 are general to consider the bulk speciation of Fe as II or III. Given the experimental conditions of our studies, both equations could be constrained for Fe(III). To model the full set of experimental data points, eq 2 was integrated and then converted to %DFe(aq) as shown in eq 3:

$$\% \text{DFe}(t) = \%[\text{H}_3\text{O}^+(\text{aq})]_0 \cdot (1 - e^{-k_1 t}) \quad (3)$$

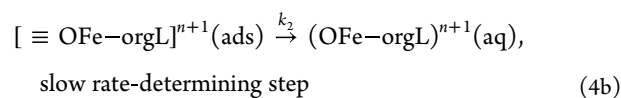
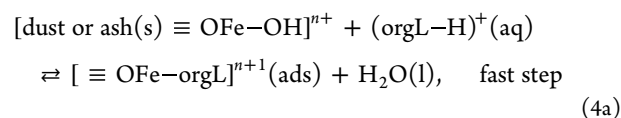
where

$$\begin{aligned} \%[\text{H}_3\text{O}^+(\text{aq})]_0 \\ = \frac{[\text{H}_3\text{O}^+(\text{aq})]_0 \cdot V_{\text{slurry}} \cdot (10^6 \mu\text{g g}^{-1}) \cdot (19 \text{ g mol}^{-1})}{m_{\text{slurry}} \cdot [\text{TE}(\text{aq})]_{\text{acid extr.}}} \times 100 \end{aligned}$$

where  $[\text{H}_3\text{O}^+(\text{aq})]_0$  is the concentration of  $\text{H}_3\text{O}^+$  (mol L<sup>-1</sup>),  $V_{\text{slurry}}$  is the volume of slurry (L),  $m_{\text{slurry}}$  is the mass of particles in the slurry (g), and  $[\text{TE}(\text{aq})]_{\text{acid extr.}}$  is trace element concentration in units of  $\mu\text{g g}^{-1}$ .

The fitting parameters in eq 3 are  $\%[\text{H}_3\text{O}^+(\text{aq})]_0$  and  $k_1$ . For obtaining the initial dissolution rate as  $t \rightarrow 0$ , eq 3 could be approximated as  $\% \text{DFe}(t) = \%[\text{H}_3\text{O}^+(\text{aq})]_0 \cdot k_1 t$ . Hence, the slope would equal  $\%[\text{H}_3\text{O}^+(\text{aq})]_0 \cdot k_1$ . Since dissolution is an interfacial process, the  $\%[\text{H}_3\text{O}^+(\text{aq})]_0$  refers to hydronium ions at the liquid/solid interface used in the derivation of surface complexation models,<sup>44</sup> not the ones measured by the pH electrode for the bulk solution.

At pH 3 with organics, ligand-promoted dissolution under acidic conditions will include reactions 1a and 1b and the following reactions:



Here, we used Ox and CAT as the organic ligands. Equation 5 is the simplified rate equation derived from reactions 1b and 4b for ligand-promoted dissolution under acidic conditions

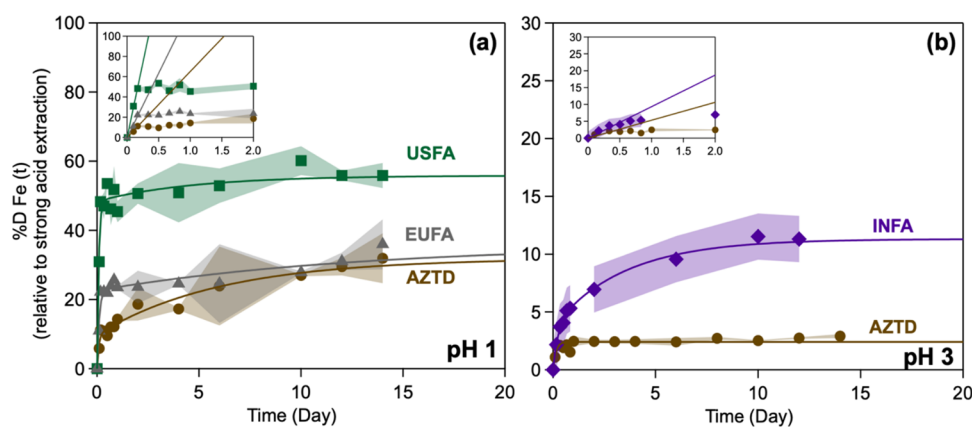


**Figure 1.** Dissolution kinetic curves of Fe expressed as %DFe(*t*) in the absence of organic compounds for (a) AZTD, EUFA, and USFA at pH 1, and (b) AZTD and INFA at pH 3, using HCl. The lines through the data are least-squares fittings using the fast and slow dissolution kinetic model as described in the text. The insets show the data points up to day 2 of the experiments, with the linear least squares as the solid lines for the initial dissolution rates. The best fit parameters are shown in Figure 4. The shaded area represents  $\pm\sigma$  from propagating error calculated from averaging 2–3 measurements.

following the same derivation approach for acid-promoted dissolution detailed in the SI:

$$\begin{aligned} \frac{d[\text{DFe}]}{dt} &= k_1 \cdot [\text{H}_3\text{O}^+(\text{aq})]_0 e^{-k_1 t} + k_2 \cdot [(\text{orgL}-\text{H})^+(\text{aq})]_0 e^{-k_2 t} \\ &= k' e^{-k_1 t} + k'' e^{-k_2 t} \end{aligned} \quad (5)$$

where  $k' = k_1[\text{H}_3\text{O}^+(\text{aq})]_0$  and  $k'' = k_2 \cdot [(\text{orgL}-\text{H})^+(\text{aq})]_0$ . When integrated to model the full set of experimental data points and then converted to %DFe(aq), eq 5 becomes

$$\begin{aligned} \% \text{DFe}(t) &= \%[\text{H}_3\text{O}^+(\text{aq})]_0 \cdot (1 - e^{-k_1 t}) \\ &+ \%[(\text{orgL}-\text{H})^+(\text{aq})]_0 \cdot (1 - e^{-k_2 t}) \end{aligned} \quad (6)$$

where

$$\begin{aligned} \%[\text{H}_3\text{O}^+(\text{aq})]_0 &= \frac{[\text{H}_3\text{O}^+(\text{aq})]_0 \cdot V_{\text{slurry}} \cdot (10^6 \mu\text{g g}^{-1}) \cdot (19 \text{ g mol}^{-1})}{m_{\text{slurry}} \cdot [\text{DM}(\text{aq})]_{\text{acid extr.}}} \times 100 \end{aligned}$$

and

$$\begin{aligned} \%[(\text{orgL}-\text{H})^+(\text{aq})]_0 &= \frac{[(\text{orgL}-\text{H})^+(\text{aq})]_0 \cdot V_{\text{slurry}} \cdot (10^6 \mu\text{g g}^{-1}) \cdot \text{MW}_{\text{org}}}{m_{\text{slurry}} \cdot [\text{DM}(\text{aq})]_{\text{acid extr.}}} \times 100 \end{aligned}$$

where  $[\text{DFe}(\text{aq})]_{\text{acid extr.}}$  is in units of  $\mu\text{g g}^{-1}$  and the molecular weights of the organic species are  $\text{MW}_{\text{org}} = 89 \text{ g mol}^{-1}$  for  $\text{HC}_2\text{O}_4^-(\text{aq})$  (the major aqueous species for Ox at pH 3) and  $110 \text{ g mol}^{-1}$  for  $\text{C}_6\text{H}_6\text{O}_2(\text{aq})$  (fully protonated CAT at pH 3).<sup>45</sup> Equation 6 is a double exponential function that describes a growth curve with two dissolution kinetic regimes: initial fast followed by slow as quantified by two rate constants,  $k_1$  and  $k_2$ , respectively. This equation has four fitting parameters, and the curve reaches a plateau at a value equivalent to the sum of  $\%[\text{H}_3\text{O}^+(\text{aq})]_0$  and  $\%[(\text{orgL}-\text{H})^+(\text{aq})]_0$ . Hence, to reduce the number of variables to three, the average experimental data points in the plateau of the %DFe(*t*) kinetic curve were calculated and used to substitute  $\%[(\text{orgL}-\text{H})^+(\text{aq})]_0$  with (plateau average  $- \%[\text{H}_3\text{O}^+(\text{aq})]_0$ ) in eq 6. Hence, the fitting parameters would be  $\%[\text{H}_3\text{O}^+(\text{aq})]_0$ ,  $k_1$ , and  $k_2$ . Similar to the approximation above for obtaining the initial dissolution rate at

pH 1, the slope would equal  $\%[\text{H}_3\text{O}^+(\text{aq})]_0 k_1$ . Introducing a third rate constant that describes the “intermediate” kinetic regime as done by Shi and co-workers<sup>31,37</sup> introduced additional fitting parameters that did not improve the output. By the definition of an exponential function, the “intermediate” kinetic region is captured in the rate constant of the “slow” kinetic region. Also, for the dissolution at pH 3, the chloride ions from using HCl to acidify the solutions will not play a significant role as reported by Cornell et al.<sup>46</sup> for the dissolution of goethite ( $\alpha\text{-FeOOH}$ ) between 0.1 and 2 N. Once DFe is in solution, the dominant aqueous species in the dark and in the presence of dissolved oxygen would be hydrated hydroxides of Fe(III),  $[\text{Fe}(\text{H}_2\text{O})_5(\text{OH})]^{2+}$ .<sup>19,33,38,47,48</sup>

## RESULTS AND DISCUSSION

### Maximum Levels of DFe from AZTD and Coal Fly Ash.

The dissolution kinetics of Fe from AZTD and coal fly ash samples INFA, USFA, and EUFA were studied over hours to 14 days at bulk pH 1 and 3 to simulate atmospheric aging under dark conditions at 298 K. Figure 1a shows the kinetic curves for %DFe at bulk pH 1 in the absence of organics, Ox, and CAT. At this pH, the dissolution is driven by proton adsorption on surface sites to a much larger extent than organic ligands. The %DFe was calculated from raw [DFe] in ppm ( $\text{mg L}^{-1}$ ) according to eq S5. The normalization of DFe levels from atmospheric aging experiments to the maximum mass-normalized DFe from strong acid extraction experiments for each solid is equivalent to normalizing the former to the surface area of the solids. Hence, a comparison in the levels of %DFe among different solid materials can be made after accounting for surface area differences affecting reactivity. Within the uncertainty of the measurements in Figure 1a, the maximum %DFe at the end of the atmospheric aging experiments at pH 1 follows this trend: USFA ( $58 \pm 15\%$ ) > EUFA  $\sim$  AZTD ( $30 \pm 15\%$ ). The latter values for EUFA and AZTD are lower than those we reported earlier in Figure 4 of ref 36 at  $150 \pm 20$  and  $85 \pm 20\%$ , respectively. Despite following the quality control and quality assurance protocols in this work and earlier reported studies in our laboratories, this difference in results is not surprising because it highlights the variability in the random error from conducting similar

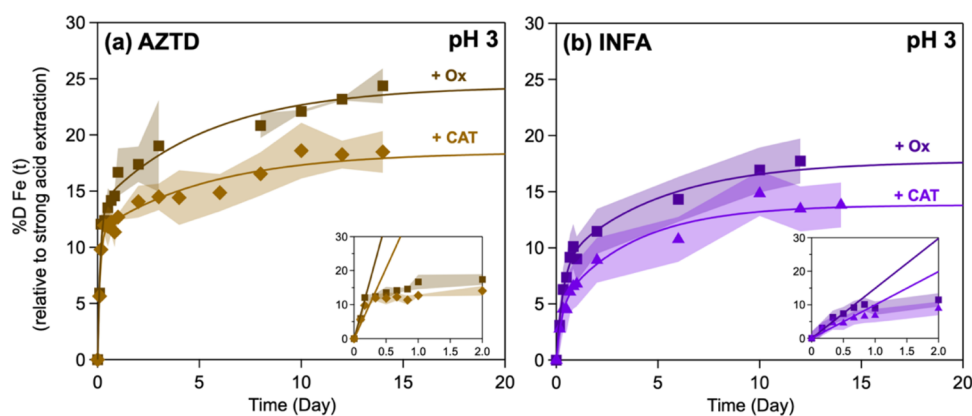


**Figure 2.** Dissolution kinetic curves of Fe expressed as %DFe(*t*) in the presence of organic compounds for (a) AZTD and (b) INFA at pH 3 using HCl. The lines through the data are least-squares fitting using double exponential kinetic functions as described in the text. The insets show the data points up to day 2 of the experiments with the linear least squares as the solid lines for the initial dissolution rates. The best fit parameters are listed in Figure 4. Ox = hydrogen oxalate, CAT = pyrocatechol. The shaded area represents  $\pm\sigma$  from propagating error calculated from averaging 2–3 measurements.

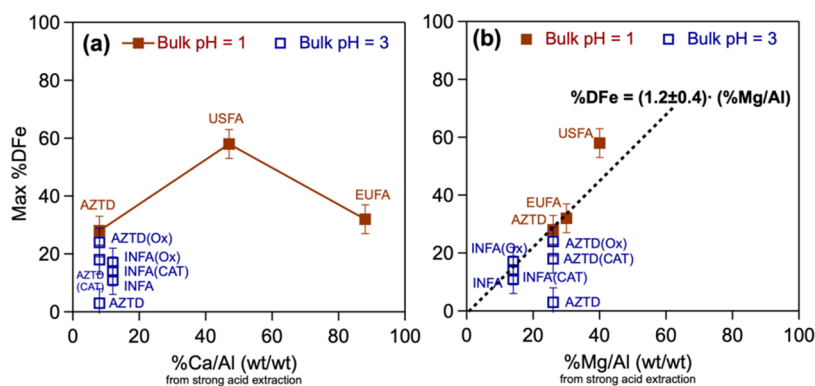


**Figure 3.** Correlation between the maximum %DFe (from Figures 1 and 2) and the maximum (a) %Ca/Al and (b) %Mg/Al (w/w) from strong acid extraction as a function of bulk pH in the absence and presence of organics. The error bars represent  $\pm\sigma$  from averaging 2–3 measurements. The dashed line in panel (b) is the least-squares linear fit described by the equation inside the figure. Ox = hydrogen oxalate, CAT = pyrocatechol.

experiments in different laboratories despite using the same starting solid materials, reaction conditions, and a calibrated analytical instrument for quantifying DFe. Also, EUFA contains a higher ratio of dissolved Fe(II)/Fe bulk than USFA<sup>42</sup> and AZTD,<sup>19</sup> which is in general more soluble than Fe(III). Although no dissolved Fe speciation experiments were performed in our studies, the results shown in Figure 1a suggest that other factors affect the solubility rate of Fe to a higher extent than dissolved Fe speciation, such as Fe(II) or Fe(III) particularly in multielement atmospheric particles. For comparison with the data at pH 3 with no organics, the maximum %DFe in Figure 1b follows this trend: INFA ( $11 \pm 3\%$ ) > AZTD ( $3 \pm 1\%$ ). These results are 10 $\times$  and 3 $\times$  higher than those reported in ref 36 at pH 3 with no organics for the same reasons mentioned above. The statistically significant reduction in the %DFe with increasing bulk pH from 1 to 3 is in line with earlier reports summarized in the Introduction section for the effect of bulk pH on %DFe under acidic conditions.

To highlight the effect of organic ligands on %DFe from the AZTD and coal fly ash sample used here, dissolution kinetic studies were conducted at bulk pH 3 for AZTD and INFA, as shown in Figure 2. At the end of the 14 days atmospheric aging experiments, the trend in the amount of %DFe from AZTD (Figure 2a) is  $24 \pm 3\%$  (with Ox) >  $18 \pm 2\%$  (with CAT).

Hence, both Ox and CAT increased the %DFe from AZTD by 8 $\times$  and 6 $\times$ , respectively, relative to acid-only with no organics at pH 3. In our earlier work,<sup>36</sup> we reported a 4 $\times$  and 7 $\times$  increase in %DFe after 14 days atmospheric aging of AZTD at pH 3 in the presence of Ox and CAT, respectively. The underlying mechanisms for the enhancement in Fe dissolution from dust and hematite due to Ox under acidic conditions was studied extensively by our group<sup>45,49,50</sup> and others, as stated above in the introduction. Briefly, Ox adsorbs on Fe sites, forming a bidentate mononuclear complex that weakens Fe–O lattice bonds. This adsorption proceeds via proton-coupled electron transfer under acidic conditions from density functional theory calculations.<sup>51</sup> In the case of CAT, it forms a bidentate binuclear complex that reduces Fe dissolution compared to that of Ox. However, ligand to metal charge transfer between CAT and Fe results in dissolution and oxidative polymerization of CAT, leading to the formation of polycatechol that darkens the color of dust and coal fly ash particles.<sup>36,40</sup>

Similarly, the trend in the amount of %DFe from INFA (Figure 2b) is  $18 \pm 2\%$  (with Ox) >  $14 \pm 2\%$  (with CAT), which is  $\sim 2\times$  and 1.3 $\times$ , respectively, relative to acid-only with no organics at pH 3. We previously reported<sup>36</sup> a 6 $\times$  increase in %DFe after 14 days atmospheric aging of INFA at pH 3 in the presence of CAT, while the data with Ox were not available at

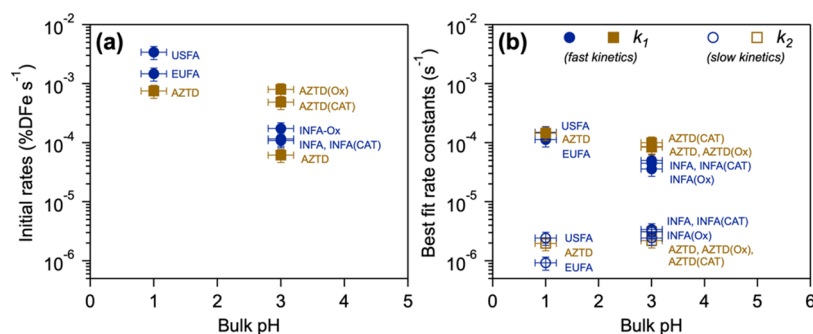


**Figure 4.** Quantifying the dissolution kinetics of Fe as a function of bulk pH from applying two methods: (a) initial rate method using the linear least-squares fitting of experimental data in the first 2 days of the atmospheric aging experiments (see insets in Figures 1 and 2) and (b) fast and slow dissolution kinetic model composed of single and double exponential functions to obtain rate constants applied to the full experimental data set of the atmospheric aging experiments (see curves in Figures 1 and 2). The error bars represent  $\pm\sigma$  from propagating error calculated from averaging 2–3 measurements. Ox = hydrogen oxalate, CAT = pyrocatechol.

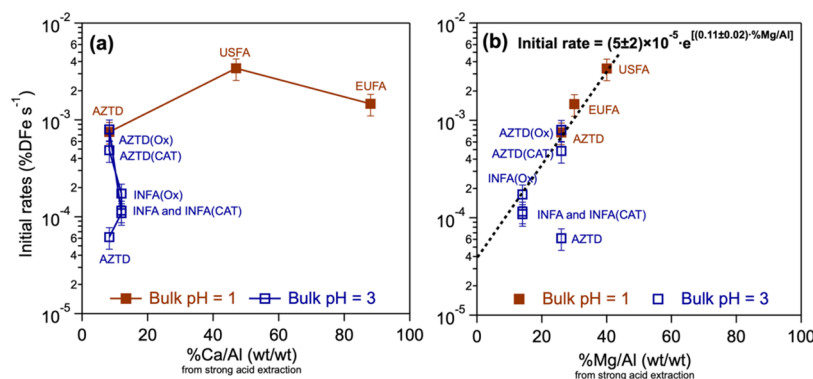


**Figure 5.** Values of initial dissolution rates of Fe as a function of the maximum (a) %Ca/Al and (b) %Mg/Al (w/w) from strong acid extraction. The rates were obtained from applying the linear least-squares fitting to the first 2 days %DFe(*t*) data from the atmospheric aging of AZTD and fly ash samples as a function of bulk pH in the absence and presence of organics shown in the insets of Figures 1 and 2. The error bars represent  $\pm\sigma$  from propagating error calculated from averaging 2–3 measurements. The dashed line in panel (b) is the least-squares fit described by the equation inside the figure. Ox = hydrogen oxalate, CAT = pyrocatechol.

pH 3 for comparison. Instead, we found that Ox enhanced %DFe by 1.3× at pH 1.<sup>36</sup> These results clearly show that mineral dust aging due to acidic reactions in the presence of organics can be as efficient as or even more efficient than a coal fly ash material in releasing similar or higher levels of DFe. This conclusion is also obtained from analyzing the initial dissolution rates and from the trend in the best fit rate constants described in the following sections.

Moreover, Figure 3 shows the correlation between the maximum amount of %DFe after 14 days of atmospheric aging with the amounts of basic minerals containing Ca and/or Mg relative to the Al content in the dust and fly ash samples used here. These percentages were calculated from the values listed in Table S1. The data in Figure 3a at bulk pH 1 show a statistically significant increase in the %DFe with increasing %Ca/Al for USFA compared to AZTD. EUFA is higher than both solids in %Ca/Al, yet its max %DFe is similar to that of AZTD. The data at pH 3 are limited to two solids, AZTD and INFA, with the latter containing a relatively higher %Ca/Al at 12% compared to 8% for the former. As stated above, the addition of organic ligands Ox and CAT increased the %DFe due to ligand-promoted dissolution.

The data in Figure 3b show an increasing linear trend for the maximum %DFe with increasing %Mg/Al at both bulk pH values 1 and 3, except for the outlier data point for AZTD at bulk pH 3. Paris et al.<sup>44</sup> reported a linear trend between the

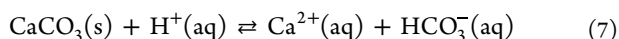
water-soluble fraction of soluble Mg and Fe extracted from dust and biomass burning aerosol collected on filters using ultrapure water with no pH adjustment. Their result was interpreted as Fe dissolution originating from clay, such as Illite or montmorillonite. To explain the results in our work, the following sections show detailed quantitative analysis of Fe dissolution kinetics for the dust and fly ash samples as a function of bulk pH, with and without organics, for correlation with the Ca and Mg content.

**Initial Dissolution Rates of Fe from AZTD and Coal Fly Ash.** The insets in Figures 1 and 2 show the experimental data points for %DFe within the first 2 days of the atmospheric aging experiments at pH 1 and 3. As stated above in the Experimental and Kinetic Modeling Methods section, the slopes, in units of %DFe s<sup>-1</sup>, would be equivalent to  $[\text{H}_3\text{O}^+(\text{aq})]_0 k_1$  according to the derivation of eqs 3 and 5. Figure 4a shows the dependence of the initial rates on the bulk pH for each of the materials used in the absence and presence of organics. Within the uncertainty of measurements, at pH 1, the trend in the initial dissolution rates of Fe decreases in this direction: USFA > EUFA > AZTD, which spans a 5× decrease between USFA and AZTD from  $(3 \pm 1) \times 10^{-3}$  to  $(8 \pm 2) \times 10^{-4}$  %DFe s<sup>-1</sup>. Upon increasing the bulk pH from 1 to 3, the initial dissolution rates decreased by nearly an order of magnitude for INFA and AZTD. In the case of INFA, the initial dissolution rate of Fe is 10<sup>-4</sup> %DFe s<sup>-1</sup> compared to

$(1.5-3) \times 10^{-3} \text{DFe s}^{-1}$  for USFA and EUFA at pH 1 (Figure 4a). This initial rate value is very close to that in the presence of CAT. The initial rate value for INFA at pH 3 increases by 2× in the presence of Ox, highlighting the effectiveness of hydrogen oxalate in enhancing the dissolution rate of Fe from coal fly ash.

In the case of AZTD, increasing the pH to 3 decreased the initial dissolution rate to  $(6 \pm 2) \times 10^{-5} \text{DFe s}^{-1}$ , nearly 13× lower than that at pH 1. However, the initial dissolution rate of Fe increased in the presence of Ox to the same level as that at pH 1. This result agrees with previous studies<sup>19,24</sup> despite differences in the experimental conditions, and highlights the effectiveness of hydrogen oxalate in enhancing the dissolution rate of Fe from mineral dust. Because these initial dissolution rates are equivalent to  $\%[\text{H}_3\text{O}^+(\text{aq})]_0 k_1$ , they are dependent on the initial concentration of the hydronium ion at the liquid/solid interface. This initial concentration will vary depending on the relative amounts of basic versus amphoteric minerals containing Ca and/or Mg, and Al and Si, respectively. Hence, as analyzed below, the trends highlighted above could either be due to similar trends in  $\%[\text{H}_3\text{O}^+(\text{aq})]_0$  or  $k_1$  from the heterogeneity of the surface sites involved in the acid- and ligand-promoted dissolution of dust and coal fly ash samples.

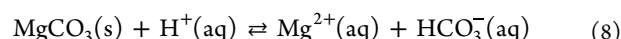
Figure 5 shows the dependence of the initial dissolution rate of Fe from AZTD and the coal fly ash samples on (a) %Ca/Al and (b) %Mg/Al calculated from mass-normalized values listed in Table S1. Contrary to an earlier study<sup>33</sup> that reported a decrease in the dissolution kinetics of Fe in the presence of CaO at pH 2, the data in Figure 5a show an increase in the initial dissolution rate at bulk pH 1 below 50% Ca/Al (USFA vs AZTD). EUFA has the highest %Ca/Al at 88%, but the initial dissolution rate of Fe is statistically lower by 2× than that for USFA (%Ca/Al = 47%). This reduction in the initial dissolution rate could be explained by a reduction in surface acidity relative to that of USFA that slowed Fe dissolution. The Ca-containing minerals identified from XRD measurements in Table 1 for EUFA were anhydrite ( $\text{CaSO}_4$ ), calcite and vaterite ( $\text{CaCO}_3$ ), and calcium aluminum oxide ( $\text{Ca}_3\text{Al}_2\text{O}_6$ ), compared to  $\text{CaSO}_4$  and  $\text{CaCO}_3$  for USFA, and albite ( $\text{Na}_{0.98}\text{Ca}_{0.02}\text{Al}_{1.02}\text{Si}_{2.98}\text{O}_8$ ) and  $\text{CaCO}_3$  in AZTD. Each of these minerals has a different reactivity in acidic solutions, with  $\text{CaCO}_3$  being the most reactive followed by much less reactive  $\text{CaSO}_4$  and calcium aluminosilicates.<sup>52,53</sup> Given this gradient in reactivity and relative amounts of Ca to Al per Table 1, the presence of basic  $\text{CaCO}_3$  in amounts lower than 50% relative to Al in these dust and coal fly ash particles would attract hydronium ions to the liquid/solid interface, hence increasing interfacial acidity to a higher extent than amphoteric  $\text{CaSO}_4$  and calcium aluminosilicates. One of the reactions that takes place with calcite would be<sup>54</sup>



The release of bicarbonate ( $\text{HCO}_3^-$ ) would relatively decrease interfacial acidity. Below 50% Ca/Al, it is likely that  $\text{HCO}_3^-$  formation does not lower interfacial acidity to a degree that inhibits Fe dissolution. However, above 50% Ca/Al as in the case of EUFA, dissolution of calcite releases higher amounts of  $\text{HCO}_3^-$  that inhibit Fe dissolution. At bulk pH 3, the dependency of the initial dissolution rate of Fe on %Ca/Al is still evident with INFA (12.5% Ca/Al) higher by ~2× than AZTD (8.4% Ca/Al) in the absence of organics. In the presence of organic ligands, Ox and CAT, the initial

dissolution rate of Fe is influenced to a larger extent by the ligand-promoted mechanism than the effect of basic minerals on interfacial acidity.

Moreover, Figure 5b shows the dependency of the initial dissolution rate of Fe from AZTD and the coal fly ash samples on %Mg/Al. There is a clear positive linear trend in the logarithmic plot of the initial dissolution rate of Fe with increasing %Mg/Al up to 40% in the materials used here corresponding to an exponential relationship between the variables. This trend is observed despite using two different bulk pH conditions that differ by 2 orders of magnitude. The reactivity of Mg-containing minerals is similar to those containing Ca, with  $\text{MgCO}_3$  being the most reactive followed by MgO and the much less reactive magnesium silicates.<sup>53</sup> It is likely that below 50% Mg/Al, the presence of basic Mg-containing minerals in the AZTD and the coal fly ash samples attracts hydronium ions to the liquid/solid interface for the following reaction to take place without significantly lowering interfacial acidity to inhibit Fe dissolution<sup>54</sup>



The only outlier data point is the initial dissolution rate of Fe from AZTD at bulk pH 3 with no organics. Interestingly, at this bulk pH, the presence of Ox and CAT increased the initial dissolution rate of Fe from AZTD to values that fall on the trend line with the %Mg/Al content. This result suggests the Mg-containing minerals cooperatively contribute to the ligand-promoted dissolution of Fe, most likely by enhancing the deprotonation of hydrogen oxalate<sup>55,56</sup> and fully protonated CAT<sup>57</sup> under acidic conditions to facilitate chelating Fe centers in the solid matrix. Since initial dissolution rates are equivalent to  $\%[\text{H}_3\text{O}^+(\text{aq})]_0 k_1$ , to disentangle the contribution of these parameters from the observed initial dissolution kinetic curves of %DFe, and to account for the fact that Fe dissolution has relatively two kinetic regimes as mentioned above, the following section describes the results from applying the fast and slow dissolution kinetic model derived in the Experimental and Kinetic Modeling Methods section for acid- and ligand-promoted dissolution kinetics of Fe, and the dependency of the best fit parameters on Ca and Mg contents of the solid materials used here.

**Dependency of the Best Fit Dissolution Rate Constants and Initial Interfacial pH on Ca and Mg Minerals.** The fast and slow dissolution kinetic model of Fe was applied to the full experimental %DFe data shown in Figures 1 and 2 covering 14 days simulated atmospheric aging as a function of bulk pH, in the absence and presence of Ox and CAT. The least-squares fitting procedure yielded three fitting parameters:  $k_1$ ,  $k_2$ , and  $\%[\text{H}_3\text{O}^+(\text{aq})]_0$ . Theoretically, rate constants are concentration-independent and their values change with changes in temperature, activation energy, or collision orientation captured in the preexponential factor of the Arrhenius equation.<sup>58</sup> Figure 4b shows the dependency of  $k_1$  and  $k_2$  on bulk pH. At pH 1, there is no statistically significant difference in  $k_1$  ( $1-2 \times 10^{-4} \text{ s}^{-1}$ ) and  $k_2$  values among the AZTD and fly ash samples ( $2.5-3 \times 10^{-6} \text{ s}^{-1}$ ), except for  $k_2$  for EUFA, which is lower by 3× than USFA and EUFA at  $10^{-6} \text{ s}^{-1}$ , suggesting that most Fe dissolution from EUFA occurred in the fast kinetic regime and the effect of mineralogy is clearer in the slow kinetic regime. At pH 3, the  $k_1$  values for AZTD with and without Ox and CAT ( $0.8-1 \times 10^{-4} \text{ s}^{-1}$ ) are statistically higher by 2× than those for INFA ( $0.3-0.6 \times 10^{-4} \text{ s}^{-1}$ ). Because  $k_1$  values are obtained from best

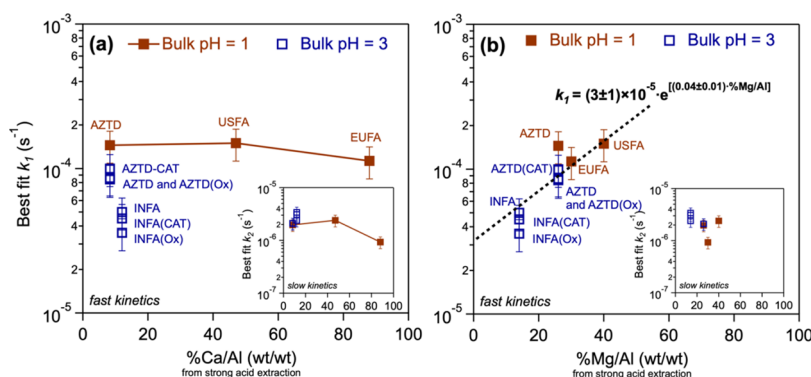


**Figure 6.** Values of best fit parameters rate constants  $k_1$  and  $k_2$  (insets) for the dark dissolution of Fe as a function of the maximum (a) %Ca/Al and (b) %Mg/Al (w/w) from strong acid extraction. The rate constants were obtained from applying the fast and slow Fe dissolution kinetics model to the full %DFe data from the atmospheric aging of AZTD and fly ash samples as a function of bulk pH in the absence and presence of organics shown in Figures 1 and 2. The error bars represent  $\pm\sigma$  from propagating error calculated from averaging 2–3 measurements. The dashed line in panel (b) is the least-squares fit described by the equation inside the figure. Ox = hydrogen oxalate, CAT = pyrocatechol.

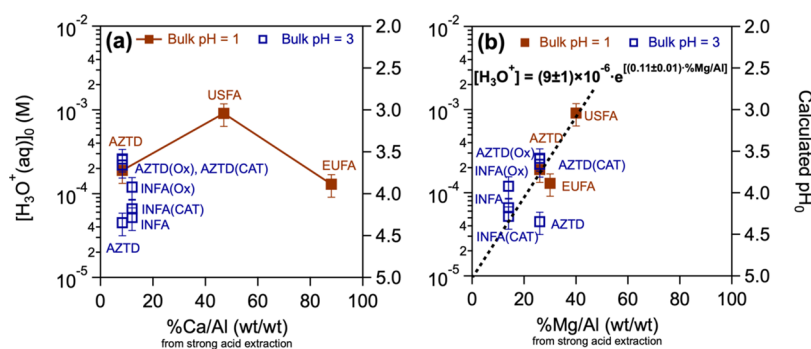


**Figure 7.** Values of best fit parameters  $[\text{H}_3\text{O}^+(\text{aq})]_0$  and the corresponding calculated  $\text{pH}_0$  as a function of the maximum (a) %Ca/Al and (b) %Mg/Al (w/w) from strong acid extraction. The values were obtained from applying the fast and slow Fe dissolution kinetics model to the full %DFe data from the atmospheric aging of AZTD and fly ash samples as a function of bulk pH in the absence and presence of organics shown in Figures 1 and 2. The error bars represent  $\pm\sigma$  from propagating error calculated from averaging 2–3 measurements. The dashed line in panel (b) is the least-squares fit described by the equation inside the figure. Ox = hydrogen oxalate, CAT = pyrocatechol.

fits to the experimental data normalized to the surface area, this difference in  $k_1$  values between AZTD and INFA stems from other factors, most likely mineralogy. The lack of statistical significance in  $k_1$  values for AZTD and INFA at bulk pH 3 with and without organics suggests that the concentration of the species at the liquid/solid interface, namely, hydronium ions and organic complexes, influences the initial dissolution rate observed in Figure 4a to a much larger degree than changes in the activation energy or collision orientation. This interpretation is supported below in the discussion of Figure 7.

Figure 6 shows the values of  $k_1$  (for the fast kinetics) and in the insets,  $k_2$  (for the slow kinetics), as a function of (a) %Ca/Al and (b) %Mg/Al. Within the propagated uncertainty of the  $k_1$  and  $k_2$  values in Figure 6a, there is no statistically significant increase with increasing %Ca/Al up to 50% at bulk pH 1. There is a statistically insignificant decrease in  $k_1$  for EUFA with %Ca/Al  $\sim$  88%. However, the drop in  $k_2$  for EUFA is statistically significant (inset of Figure 6a). This result suggests that the trend observed for the initial dissolution rate with %Ca/Al shown in Figure 5a is influenced to a larger extent by  $[\text{H}_3\text{O}^+(\text{aq})]_0$  than  $k_1$ , which is indeed the case as shown in Figure 7a for the trend in  $[\text{H}_3\text{O}^+(\text{aq})]_0$  with %Ca/Al. At bulk pH 3, there is a statistically significant decrease in  $k_1$  values (Figure 6a) for INFA relative to AZTD with increasing %Ca/Al likely due to the presence of less reactive Ca-containing minerals toward Fe dissolution. The values of  $k_1$  and  $k_2$  for

ligand-promoted dissolution kinetics at bulk pH 3 with Ox and CAT are within the error of those in the absence of the organics for both INFA and AZTD. Hence, the pronounced effect of the ligands Ox and CAT on the initial dissolution rate shown in Figure 5 is mainly due to their role in increasing the  $[\text{H}_3\text{O}^+(\text{aq})]_0$  as shown in Figure 7a.

The right y-axis in Figure 7 is for the initial interfacial  $\text{pH}_0$  (calculated from  $[\text{H}_3\text{O}^+(\text{aq})]_0$ ), which ranges from 3.0 to 4.5. These values are higher than the bulk pH 1 and 3 measured for the slurries containing AZTD and the fly ash samples during the simulated atmospheric aging experiments. The difference between the calculated  $\text{pH}_0$  and measured bulk pH is expected due to the formation of bicarbonate from basic Ca- and Mg-carbonate under acidic solution conditions, hence raising the pH, as shown in reactions 7 and 8. Within the uncertainty of the best fit  $k_1$  values in Figure 6b for the fast dissolution kinetics, there is an increasing linear trend with increasing %Mg/Al for the AZTD and coal fly ash used here at bulk pH 1 and 3 in the logarithmic plot of  $k_1$  versus %Mg/Al corresponding to an exponential relationship between the variables, whereas no trend is observed for  $k_2$  in the inset. The outlier to this linear trend is from  $k_1$  of AZTD (no organics) at pH 1. These data suggest that the presence of basic Mg minerals within the solid samples studied here at levels below 50% Mg/Al enhance the dissolution kinetics of Fe under acidic conditions in the absence and presence of organics. The 1

order of magnitude difference in  $k_1$  values in the 14–40% Mg/Al stems from the heterogeneity of Mg minerals in these samples (Table 1).

The trend in  $k_1$  values with increasing %Mg/Al would partially explain the trend observed for the initial dissolution rate, equivalent to  $\%[\text{H}_3\text{O}^+(\text{aq})]_0 k_1$ , with %Mg/Al shown in Figure 6b. Mg minerals would also affect the  $\%[\text{H}_3\text{O}^+(\text{aq})]_0 k_1$  at the liquid/solid interface. Figure 7b shows an increase in the best fit  $\%[\text{H}_3\text{O}^+(\text{aq})]_0$  with increasing %Mg/Al, and hence an increase in surface acidity (i.e., lower calculated  $\text{pH}_0$ , right axis). There are a few outliers to this linear trend, most notably AZTD and INFA(Ox) from bulk pH 3 experiments. As stated above when explaining the data in Figure 5b, basic Mg minerals are more reactive than Mg aluminosilicates and hence would attract hydronium ions to the liquid/solid interface and facilitate the deprotonation of Ox and CAT needed to promote acid- and ligand-Fe dissolution.

## CONCLUSIONS

The results reported here aim to quantify the dissolution rates of Fe from the aging of fully characterized multielement dust and fly ash under acidic conditions (bulk pH 1 or 3) in the dark, with and without oxalic acid and pyrocatechol. The coal fly ash contained relatively higher amounts of Ca and Mg than AZTD. At bulk pH 1, there is a statistically significant increase in the maximum %DFe with increasing %Ca/Al and %Mg/Al below 50%. The presence of organics representative of dicarboxylic acid and polyphenols affected the %DFe to a higher degree than the Ca and Mg contents in the solids. The initial dissolution rates of Fe increased exponentially with %Ca/Al and %Mg/Al below 50% but decreased with %Ca/Al higher than 50%. The best fit parameters from the fast and slow dissolution kinetic model revealed that reactive Ca and Mg minerals increased the calculated initial pH at the liquid/solid interface to values higher by only 1.5–2 units than the measured bulk pH due to bicarbonate formation. The data also suggested that reactive Ca and Mg minerals enhanced the deprotonation of hydrogen oxalate and pyrocatechol at the liquid/solid interface, which aided in ligand-promoted dissolution of Fe. The kinetic results clearly showed that mineral dust aging due to acidic reactions in the presence of organics can be as efficient as the fresh coal fly ash material in releasing equivalent amounts of DFe.

Our results highlight the importance of multielemental analysis of atmospheric aerosol particles to quantifying the maximum amount and dissolution kinetics of trace elements like Fe. The particles we used cover a wide range of maximum total extractable Ca/Al and Mg/Al ratios. Hence, for atmospheric particles collected on filters, if a portion of the filters was subjected to strong acid extraction to quantify Fe, Al, Ca, and Mg, the levels of these elements could be used to calculate %DFe, %Ca/Al, and %Mg/Al from the leaching experiments on the other portion of the filters, without the need to know the surface area of the collected particles. Ideally, leaching experiments should be done for 1 day using Millipore water under acidic pH 3, which is not too low to cause additional dissolution beyond atmospheric aging and not too high to cause precipitation of Fe hydroxides. Based on this method, the extent of aging of the collected particles could be inferred when the results are compared to the data from the standard materials used here. In addition, the results reported here could serve as the basis for future experimental and modeling studies aimed at quantifying the magnitude of the

change in the Fe dissolution kinetic parameters due to changes in the temperature, ionic strength, and solar irradiation of atmospheric relevance. Future experimental, speciation modeling, and computational chemistry work is needed to measure and estimate interfacial pH of mixed minerals and metal oxides for comparison with bulk pH to constrain kinetic dissolution models with the neutralizing effect of basic Ca and Mg minerals.

## ASSOCIATED CONTENT

### Supporting Information

The Supporting Information is available free of charge at <https://pubs.acs.org/doi/10.1021/acs.jpca.4c05181>.

Selected dissolved Fe and crustal elements from strong acid extraction experiments, details on methods, and derivation of the dissolution kinetics modeling (Table S1) (PDF)

## AUTHOR INFORMATION

### Corresponding Authors

Hind A. Al-Abadleh – Department of Chemistry and Biochemistry, Wilfrid Laurier University, Waterloo, Ontario N2L 3C5, Canada; Present Address: Department of Earth, Environmental and Resource Sciences, University of Texas at El Paso, 500 West University Avenue, El Paso, Texas 79902, United States; [orcid.org/0000-0002-9425-0646](https://orcid.org/0000-0002-9425-0646); Phone: (915)747-5501; Email: [haalabadleh@utep.edu](mailto:haalabadleh@utep.edu); Fax: (915)747-5073

Nausheen W. Sadiq – Department of Chemistry and Physics, Mount Royal University, Calgary, Alberta T3E 6K6, Canada; Phone: (403)440-8933; Email: [nsadiq@mtroyal.ca](mailto:nsadiq@mtroyal.ca); Fax: (403)440-8898

### Authors

Madison Smith – Department of Chemistry and Physics, Mount Royal University, Calgary, Alberta T3E 6K6, Canada

Arden Ogilvie – Department of Chemistry and Physics, Mount Royal University, Calgary, Alberta T3E 6K6, Canada

Complete contact information is available at: <https://pubs.acs.org/10.1021/acs.jpca.4c05181>

### Notes

The authors declare no competing financial interest.

## ACKNOWLEDGMENTS

N.W.S. acknowledges funding and support from Mount Royal University and Burgener Research Inc. for the contribution of Mira Mist and Ari Mist Nebulizers for this study. H.A.A. acknowledges funding from the NSERC Discovery Program. The authors thank Professor Juan Navea from Skidmore College for sharing the coal fly ash samples from his lab and Victoria Jarvis and Suha Saleem in the MAX Diffraction Facility at McMaster University for the analysis of XRD data.

## REFERENCES

- (1) Jacob, D. J. *Introduction to Atmospheric Chemistry*; Princeton University Press, 1999.
- (2) Griffin, D. W.; Kellogg, C. A.; Shinn, E. A. Dust in the Wind: Long Range Transport of Dust in the Atmosphere and Its Implications for Global Public and Ecosystem Health. *Global Change Human Health* **2001**, *2*, 20–33.
- (3) Tilgner, A.; Schaefer, T.; Alexander, B.; Barth, M. C.; Collett, J. L., Jr.; Fahey, K. M.; Nenes, A.; Pye, H. O. T.; Herrmann, H.;

- McNeill, V. F. Acidity and the multiphase chemistry of atmospheric aqueous particles and clouds. *Atmos. Chem. Phys.* **2021**, *21*, 13483–13536.
- (4) Al-Abadleh, H. A. Iron content in aerosol particles and its impact on atmospheric chemistry. *Chem. Commun.* **2024**, *60*, 1840–1855.
- (5) Abbatt, J. P. D.; Ravishankara, A. R. Opinion: Atmospheric multiphase chemistry – past, present, and future. *Atmos. Chem. Phys.* **2023**, *23*, 9765–9785.
- (6) Pye, H. O. T.; Nenes, A.; Alexander, B.; Ault, A. P.; Barth, M. C.; Clegg, S. L.; Collett, J. L., Jr.; Fahey, K. M.; Hennigan, C. J.; Herrmann, H.; et al. The acidity of atmospheric particles and clouds. *Atmos. Chem. Phys.* **2020**, *20*, 4809–4888.
- (7) Herrmann, H.; Schaefer, T.; Tilgner, A.; Styler, S. A.; Weller, C.; Teich, M.; Otto, T. Tropospheric Aqueous-Phase Chemistry: Kinetics, Mechanisms, and Its Coupling to a Changing Gas Phase. *Chem. Rev.* **2015**, *115*, 4259–4334.
- (8) Al-Abadleh, H. A.; Nizkorodov, S. A. Open Questions on Transition Metals Driving Secondary Thermal Processes in Atmospheric Aerosols. *Commun. Chem.* **2021**, *4*, No. 176.
- (9) Al-Abadleh, H. A.; Kubicki, J. D.; Meskhidze, N. A perspective on iron (Fe) in the atmosphere: air quality, climate, and the ocean. *Environ. Sci.: Processes Impacts* **2023**, *25*, 151–164.
- (10) Hamilton, D. S.; Scanza, R. A.; Feng, Y.; Guinness, J.; Kok, J. F.; Li, L.; Liu, X.; Rathod, S. D.; Wan, J. S.; Wu, M.; Mahowald, N. M. Improved methodologies for Earth system modelling of atmospheric soluble iron and observation comparisons using the mechanism of Intermediate complexity for Modelling Iron (MIMI v1.0). *Geosci. Model Dev.* **2019**, *12*, 3835–3862.
- (11) Mahowald, N. M.; Scanza, R. A.; Brahney, J.; Goodale, C. L.; Hess, P. G.; Moore, J. K.; Neff, J. Aerosol Deposition Impacts on Land and Ocean Carbon Cycles. *Curr. Clim. Change Rep.* **2017**, *3*, 16–31.
- (12) Meskhidze, N.; Volker, C.; Al-Abadleh, H. A.; Barbeau, K.; Bressac, M.; Buck, C.; Bundy, R. M.; Croot, P. L.; Feng, Y.; Ito, A.; et al. Perspective on identifying and characterizing the processes controlling iron speciation and residence time at the atmosphere-ocean interface. *Mar. Chem.* **2019**, *217*, No. 103704.
- (13) Baker, A. R.; Kanakidou, M.; Nenes, A.; Myriokefalitakis, S.; Croot, P.; Duce, R. A.; Gao, Y.; Guieu, C.; Ito, A.; Jickells, T. D.; et al. Changing atmospheric acidity as a modulator of nutrient deposition and ocean biogeochemistry. *Sci. Adv.* **2021**, *7*, No. eabd8800.
- (14) Liss, P. S.; Johnson, M. T. Ocean-Atmosphere Interactions of Gases and Particles. In *Springer Earth System Sciences*; Springer: Heidelberg, 2014.
- (15) Mahowald, N. M.; Hamilton, D. S.; Mackey, K. R. M.; Moore, J. K.; Baker, A. R.; Scanza, R. A.; Zhang, Y. Aerosol trace metal leaching and impacts on marine microorganisms. *Nat. Commun.* **2018**, *9*, No. 2614.
- (16) Wurl, O.; Ekau, W.; Landing, W. M.; Zappa, C. J. Sea surface microlayer in a changing ocean – A perspective. *Elem.: Sci. Anthropocene* **2017**, *5*, No. 31.
- (17) Kanakidou, M.; Myriokefalitakis, S.; Tsigaridis, K. Aerosols in atmospheric chemistry and biogeochemical cycles of nutrients. *Environ. Res. Lett.* **2018**, *13*, No. 063004.
- (18) Perron, M. M. G.; Fietz, S.; Hamilton, D. S.; Ito, A.; Shelley, R. U.; Tang, M. Preface to the inter-journal special issue “RUSTED: Reducing Uncertainty in Soluble aerosol Trace Element Deposition. *Atmos. Meas. Tech.* **2024**, *17*, 165–166.
- (19) Chen, H.; Grassian, V. H. Iron Dissolution of Dust Source Materials during Simulated Acidic Processing: The Effect of Sulfuric, Acetic, and Oxalic Acids. *Environ. Sci. Technol.* **2013**, *47*, 10312–10321.
- (20) Rubasinghege, G.; Lentz, R. W.; Scherer, M. M.; Grassian, V. H. Simulated atmospheric processing of iron oxyhydroxide minerals at low pH: Roles of particle size and acid anion in iron dissolution. *Proc. Natl. Acad. Sci. U.S.A.* **2010**, *107*, 6628–6633.
- (21) Chen, H.; Laskin, A.; Baltrusaitis, J.; Gorski, C. A.; Scherer, M. M.; Grassian, V. H. Coal Fly Ash as a Source of Iron in Atmospheric Dust. *Environ. Sci. Technol.* **2012**, *46*, 2112–2120.
- (22) Buck, C. S.; Landing, W. M.; Resing, J. A. Particle size and aerosol iron solubility: A high-resolution analysis of Atlantic aerosols. *Mar. Chem.* **2010**, *120*, 14–24.
- (23) Meskhidze, N.; Hurley, D.; Royalty, T. M.; Johnson, M. S. Potential effect of atmospheric dissolved organic carbon on the iron solubility in seawater. *Mar. Chem.* **2017**, *194*, 124–132.
- (24) Paris, R.; Desboeufs, K. Effect of atmospheric organic complexation on iron-bearing dust solubility. *Atmos. Chem. Phys.* **2013**, *13*, 4895–4905.
- (25) Wozniak, A. S.; Shelley, R. U.; McElhenie, S. D.; Landing, W. M.; Hatcher, P. G. Aerosol water soluble organic matter characteristics over the North Atlantic Ocean: Implications for iron-binding ligands and iron solubility. *Mar. Chem.* **2015**, *173*, 162–172.
- (26) Journet, E.; Desboeufs, K.; Caquineau, S.; Colin, J.-L. Mineralogy as a critical factor of dust iron solubility. *Geophys. Res. Lett.* **2008**, *35*, L07805.
- (27) Rubasinghege, G.; Lentz, R. W.; Park, H.; Scherer, M. M.; Grassian, V. H. Nanorod Dissolution Quenched in the Aggregated State. *Langmuir* **2010**, *26*, 1524–1527.
- (28) Fang, T.; Guo, H.; Zeng, L.; Verma, V.; Nenes, A.; Weber, R. J. Highly Acidic Ambient Particles, Soluble Metals, and Oxidative Potential: A Link between Sulfate and Aerosol Toxicity. *Environ. Sci. Technol.* **2017**, *51*, 2611–2620.
- (29) McDaniel, M. F. M.; Ingall, E. D.; Morton, P. L.; Castorina, E.; Weber, R. J.; Shelley, R. U.; Landing, W. M.; Longo, A. F.; Feng, Y.; Lai, B. Relationship between Atmospheric Aerosol Mineral Surface Area and Iron Solubility. *ACS Earth Space Chem.* **2019**, *3*, 2443–2451.
- (30) Ito, A.; Myriokefalitakis, S.; Kanakidou, M.; Mahowald, N.; Scanza, R. A.; Hamilton, D. S.; Baker, A. R.; Jickells, T. D.; Sarin, M.; Bikina, S.; et al. Pyrogenic iron: The missing link to high iron solubility in aerosols. *Sci. Adv.* **2019**, *5*, No. eaau7671.
- (31) Baldo, C.; Ito, A.; Krom, M. D.; Li, W.; Jones, T.; Drake, N.; Ignatyev, K.; Davidson, N.; Shi, Z. Iron from coal combustion particles dissolves much faster than mineral dust under simulated atmospheric acidic conditions. *Atmos. Chem. Phys.* **2022**, *22*, 6045–6066.
- (32) Ito, A. Atmospheric Processing of Combustion Aerosols as a Source of Bioavailable Iron. *Environ. Sci. Technol. Lett.* **2015**, *2*, 70–75.
- (33) Hettiarachchi, E.; Reynolds, R. L.; Goldstein, H. L.; Moskowitz, B.; Rubasinghege, G. Iron dissolution and speciation in atmospheric mineral dust: Metal-metal synergistic and antagonistic effects. *Atmos. Environ.* **2018**, *187*, 417–423.
- (34) Hettiarachchi, E.; Rubasinghege, G. Mechanistic Study on Iron Solubility in Atmospheric Mineral Dust Aerosol: Roles of Titanium, Dissolved Oxygen, and Solar Flux in Solutions Containing Different Acid Anions. *ACS Earth Space Chem.* **2020**, *4*, 101–111.
- (35) Hettiarachchi, E.; Hurab, O.; Rubasinghege, G. Atmospheric Processing and Iron Mobilization of Ilmenite: Iron-Containing Ternary Oxide in Mineral Dust Aerosol. *J. Phys. Chem. A* **2018**, *122*, 1291–1302.
- (36) Sadiq, N. W.; Venter, C.; Mohammed, W.; Khalaf, Y.; Al-Abadleh, H. A. Dissolution of selected trace elements from simulated atmospheric aerosol aging and human exposure of mineral dust and coal fly ash. *ES&T Air* **2024**, *1*, 5–15.
- (37) Shi, Z.; Bonneville, S.; Krom, M. D.; Carslaw, K. S.; Jickells, T. D.; Baker, A. R.; Benning, L. G. Iron dissolution kinetics of mineral dust at low pH during simulated atmospheric processing. *Atmos. Chem. Phys.* **2011**, *11*, 995–1007.
- (38) Szady, C.; Picarillo, G.; Davis, E. J.; Drapanauskaite, D.; Buneviciene, K.; Baltrusaitis, J.; Navea, J. G. Iron dissolution and speciation from combustion particles under environmentally relevant conditions. *Environ. Chem.* **2023**, *20*, 171–182.
- (39) Li, R.; Panda, P. P.; Chen, Y.; Zhu, Z.; Wang, F.; Zhu, Y.; Meng, H.; Ren, Y.; Kumar, A.; Tang, M. Aerosol trace element solubility determined using ultrapure water batch leaching: an intercomparison study of four different leaching protocols. *Atmos. Meas. Tech.* **2024**, *17*, 3147–3156.

(40) Link, N.; Removski, N.; Yun, J.; Fleming, L.; Nizkorodov, S. A.; Bertram, A. K.; Al-Abadleh, H. A. Dust-Catalyzed Oxidative Polymerization of Catechol under Acidic Conditions and its Impacts on Ice Nucleation Efficiency and Optical Properties. *ACS Earth Space Chem.* **2020**, *4*, 1127–1139.

(41) Borgatta, J.; Paskavitz, A.; Kim, D.; Navea, J. G. Comparative evaluation of iron leach from fly ash from different source regions under atmospherically relevant conditions. *Environ. Chem.* **2016**, *13*, 902–912.

(42) Kim, D.; Xiao, Y.; Karchere-Sun, R.; Richmond, E.; Ricker, H. M.; Leonardi, A.; Navea, J. G. Atmospheric Processing of Anthropogenic Combustion Particles: Effects of Acid Media and Solar Flux on the Iron Mobility from Fly Ash. *ACS Earth Space Chem.* **2020**, *4*, 750–761.

(43) de Mello Gabriel, G. V.; Pitombo, L. M.; Rosa, L. M. T.; Navarrete, A. A.; Botero, W. G.; do Carmo, J. B.; de Oliveria, L. C. The environmental importance of iron speciation in soils: evaluation of classic methodologies. *Environ. Monit. Assess.* **2021**, *193*, No. 63, DOI: 10.1007/s10661-021-08874-w.

(44) Paris, R.; Desboeufs, K.; Formenti, P.; Nava, S.; Chou, C. Chemical characterisation of iron in dust and biomass burning aerosols during AMMA-SOP0/DABEX: implication for iron solubility. *Atmos. Chem. Phys.* **2010**, *10*, 4273–4282.

(45) Situm, A.; Rahman, M. A.; Goldberg, S.; Al-Abadleh, H. A. Spectral Characterization and Surface Complexation Modeling of Organics on Hematite Nanoparticles: Role of Electrolytes in the Binding Mechanism. *Environ. Sci.: Nano* **2016**, *3*, 910–926.

(46) Cornell, R. M.; Posner, A. M.; Quirk, J. P. Kinetics and mechanisms of the acid dissolution of goethite (α-FeOOH). *J. Inorg. Nucl. Chem.* **1976**, *38*, 563–567.

(47) Stefánsson, A. Iron(III) Hydrolysis and Solubility at 25 °C. *Environ. Sci. Technol.* **2007**, *41*, 6117–6123.

(48) Lim, M.; Chiang, K.; Amal, R. Photochemical synthesis of chlorine gas from iron(III) and chloride solution. *J. Photochem. Photobiol., A* **2006**, *183*, 126–132.

(49) Al-Abadleh, H. A. Aging of atmospheric aerosols and the role of iron in catalyzing brown carbon formation. *Environ. Sci.: Atmos.* **2021**, *1*, 297–345.

(50) Augustine, L. J.; Tamijani, A. A.; Bjorklund, J. L.; Al-Abadleh, H. A.; Mason, S. E. Adsorption of Small Organic Acids and Polyphenols on Hematite Surfaces: Density Functional Theory + Thermodynamics Analysis. *J. Colloid Interface Sci.* **2022**, *609*, 469–481.

(51) Zhan, G.; Fang, Y.; Zhang, M.; Cao, S.; Xu, T.; Ling, C.; Gu, H.; Liu, X.; Zhang, L. Oxalate promoted iron dissolution of hematite via proton coupled electron transfer. *Environ. Sci.: Nano* **2022**, *9*, 1770–1779.

(52) Schuttlefield, J.; Rubasinghe, G.; El-Maazawi, M.; Bone, J.; Grassian, V. H. Photochemistry of Adsorbed Nitrate. *J. Am. Chem. Soc.* **2008**, *130*, 12210–12211.

(53) Brantley, S. L. Kinetics of Mineral Dissolution. In *Kinetics of Water-Rock Interactions*; Springer, 2008; pp 151–210.

(54) Pokrovsky, O. S.; Golubev, S. V.; Schott, J. Dissolution kinetics of calcite, dolomite and magnesite at 25 °C and 0 to 50 atm pCO<sub>2</sub>. *Chem. Geol.* **2005**, *217*, 239–255.

(55) Tang, C. Y.; Huang, Z.; Allen, H. C. Binding of Mg<sup>2+</sup> and Ca<sup>2+</sup> to palmitic acid and deprotonation of the COOH headgroup studied by vibrational sum frequency generation spectroscopy. *J. Phys. Chem. B* **2010**, *114*, 17068–17076.

(56) Faboya, O. O. The interaction between oxalic acid and divalent ions—Mg<sup>2+</sup>, Zn<sup>2+</sup> and Ca<sup>2+</sup>—in aqueous medium. *Food Chem.* **1990**, *38*, 179–187.

(57) Kim, Y. J.; Wu, W.; Chun, S.-E.; Whitacre, J. F.; Bettinger, C. J. Catechol-Mediated Reversible Binding of Multivalent Cations in Eumelanin Half-Cells. *Adv. Mater.* **2014**, *26*, 6572–6579.

(58) Atkins, P. W.; de Paula, J. *Physical Chemistry*; W. H. Freeman and Company, 2008.